# Differential scaling between G1 protein production and cell size dynamics promotes commitment to the cell division cycle in budding yeast

Litsios, Athanasios; Huberts, Daphne H E W; Terpstra, Hanna M; Guerra, Paolo; Schmidt, Alexander; Buczak, Katarzyna; Papagiannakis, Alexandros; Rovetta, Mattia; Hekelaar, Johan; Hubmann, Georg

*Published in:*
Nature Cell Biology

*DOI:*
10.1038/s41556-019-0413-3



*Publication date:*
2019

# Differential scaling between G1 protein production and cell size dynamics promotes commitment to the cell division cycle in budding yeast

**Athanasios Litsios[1], Daphne H. E. W. Huberts[1,2], Hanna Terpstra[1], Paolo Guerra[1], Alexander Schmidt[3], Katarzyna Buczak[3], Alexandros Papagiannakis[1], Mattia Rovetta[1], Johan Hekelaar[1], Georg Hubmann[1,4], Marten Exterkate[1,5], Andreas Milias-Argeitis[1,6], Matthias Heinemann[1,6,*]**

[1]Molecular Systems Biology
Groningen Biomolecular Sciences and Biotechnology Institute, University of Groningen, Nijenborgh 4, 9747 AG Groningen, Netherlands

[2]Present address: Cancer Research UK Cambridge Institute
University of Cambridge, Li Ka Shing Centre, Robinson Way, Cambridge CB2 0RE, UK

[3]Proteomics Core Facility
Biozentrum, University of Basel, 4056 Basel, Switzerland

[4]Present address: Department of Biology, Laboratory of Molecular Cell Biology, Institute of Botany and Microbiology, KU Leuven, & Center for Microbiology, VIB, Kasteelpark Arenberg, 31, 3001 Heverlee, Belgium

[5]Present address: Molecular Microbiology,
Groningen Biomolecular Sciences and Biotechnology Institute, University of Groningen, Nijenborgh 7, 9747 AG Groningen, Netherlands

[6]Correspondending authors

[*]Lead contact: m.heinemann@rug.nl

## ABSTRACT

In the unicellular eukaryote *Saccharomyces cerevisiae*, Cln3-CDK activity enables Start, the irreversible commitment to the cell division cycle. However, the concentration of Cln3 has been paradoxically considered to remain constant during G1, due to the presumed scaling of its production rate with cell size dynamics. Measuring metabolic and biosynthetic activity during cell cycle progression in single cells, we found that cells exhibit pulses in protein production rate, which do not scale with cell size dynamics, but, following the intrinsic metabolic dynamics, peak around Start. Using a viral-based bicistronic construct and targeted proteomics to measure Cln3 at the single-cell and population levels, we show that the differential scaling between protein production and cell size leads to a temporal increase in Cln3 concentration, and passage through Start. This differential scaling causes Start in both daughter and mother cells across growth conditions. Thus, uncoupling between two fundamental physiological parameters drives cell cycle commitment.


## INTRODUCTION

The cell division cycle is the process by which eukaryotic cells replicate themselves. Cells irreversibly commit to enter the cell cycle after passing through a checkpoint located in late G1, known as Start in budding yeast, or the restriction point in mammals[1]. The most upstream activator of Start is Cln3[2–4], a highly unstable G1 cyclin[5]. In complex with the cyclin-dependent kinase Cdc28, Cln3 activates Start by de-repressing SBF/MBF-related transcription via phosphorylation of the transcriptional inhibitor Whi5[6,7] and also via Whi5-independent means[8]. Cln3-mediated de-repression of transcription leads to the activation of a positive feedback loop involving SBF and the late G1 cyclins Cln1/2, which locks the transition from the G1 to the S phase of the cell cycle[9].

Although it has long been known that Cln3 overexpression triggers early passage through Start, and thus, Cln3 is a rate-limiting activator of Start[2–4], the dynamics of Cln3 protein concentration during the cell cycle are still largely enigmatic. While the mRNA of CLN3 appears to oscillate during the cell cycle, with a peak around the M/G1 transition[4,10], the dynamics of the Cln3 protein are unclear. Early bulk measurements with cells from synchronous cultures suggested that there are no cell-cycle related fluctuations in Cln3 levels[4]. However, later population-level studies pointed towards changes in Cln3 abundance during G1[11,12]. Determination of Cln3 levels via microscopy has so far remained impossible, likely due to the instability of the protein[5] and its low abundance. Time-lapse microscopy with hyperstable Cln3 mutants, however, suggested that the concentration of Cln3 remains constant during G1[13]. Thus, despite its key position in the Start network, the dynamics of this critical cell cycle regulator remain elusive.

The abundance of Cln3 is considered to be directly dependent on the rate of protein production[14], due to the instability of Cln3 and the sensitivity of its translation rate to overall translation initiation[15]. However, the dynamics of the protein production rate and cell size during G1 are also still rather elusive, and thus, it is unclear how they together influence the concentration of Cln3. It is generally assumed that protein production rate scales with cell size[14], according to which the concentration of Cln3 would remain constant during the cell cycle[13,16]. However, it is unclear whether this parallel scaling is correct: while the rate of protein production has been described to either increase exponentially during the cell cycle[17,18] or to remain constant[19], the rate of cell size increase has been found to be exponential[20,21], biphasic with two distinct linear growth phases[19], or even to have more complex dynamics[22,23]. Thus, despite being fundamental physiological parameters, the dynamics of the protein production rate and cell size during the cell cycle, and thus, their relationship and effect on Cln3 dynamics, remain unclear.

Despite the ambiguity in Cln3 dynamics, all prevalent models for Start assume a constant Cln3 concentration during G1[8,13,24,25]. For instance, it was suggested that with constant Cln3 concentration, the increase in the absolute number of Cln3 molecules during G1 would promote Start by saturating a fixed number of SBF binding sites[8]. However, more recent work suggested that the ratio between Cln3 and Whi5 levels is what determines Start independently of DNA content[13]. Alternatively, it was proposed that release of ER-retained Cln3 during G1 leads to an increase in nuclear Cln3 concentration and promotion of Start[24,25]. However, a recent localization analysis with a hyperstable Cln3 mutant did not show any change in the enrichment of Cln3 in the nucleus during G1[13]. Finally, also assuming a constant Cln3 concentration, it was proposed that Start is triggered by the dilution of the Start-inhibitor Whi5[13]. However, a recent study did not detect any decrease in Whi5 concentration during G1[26]. Moreover, while the Whi5-dilution model assumes that the increase of cell size during G1 determines the timing of Start, a lack of correlation between the rate of cell proliferation and cell size was recently reported[27], leaving unclear how the respective model applies across growth conditions.

A so far underrated element of Start control is the intrinsic dynamics of metabolism during the cell cycle[28,29]. Metabolic oscillations in the hour-scale, although autonomous from the cell cycle[29,30], are strongly coupled to cell cycle progression across growth conditions[29,31], with the period around Start being characterized by an increase in flux through central carbon metabolism[32]. Metabolism is linked to Start, at least partially, via acetyl-CoA, a metabolite of glucose catabolism, which induces the transcription of CLN3 along with ribosomal and other growth genes through promotion of histone acetylation[33]. Also, it was suggested that metabolic inputs may shape cell cycle decisions by influencing the rate of protein production[34]. Nevertheless, it was only until recently that indication was obtained

that metabolic oscillations dynamically gate Start[29], but how metabolic oscillations influence the commitment to the division cycle remains largely unknown.

Here, using microfluidics and time-lapse microscopy to measure simultaneously cell cycle, biosynthetic, and metabolic activity in individual *Saccharomyces cerevisiae* cells, we found that at constant nutrient conditions cells display a pulse in protein production rate during G1, which (i) requires a sufficient flux through central carbon metabolism, (ii) does not scale with cell size dynamics, and (iii) is essential for passage through Start. Using a viral-based bicistronic construct to overcome the chronic technical hurdle of determining the concentration of wild type Cln3 *in vivo*, and targeted proteomics, we show that this differential scaling between protein production rate and cell size dynamics leads to a severalfold increase in Cln3 concentration in G1, causing Start. Moreover, we demonstrate that this differential scaling explains Start across different growth conditions and in both daughter and mother cells. Our results resolve a nearly two-decade long enigma, showing that the uncoupling of two fundamental physiological parameters promotes the commitment to the cell division cycle.

## RESULTS

### Cells with low glycolytic flux generate biomass, but fail to pass Start

Towards understanding the impact of metabolic oscillations on cell cycle control, we first asked if Start depends on the level of flux through central carbon metabolism. To test this, we used microfluidics[35,36] and microscopy to monitor the budding activity of hundreds of individual cells of a strain (TM6*) that, compared to wild type, displays a ≈5-fold reduced glycolytic flux in glucose-rich conditions, due to the expression of only a chimeric hexose transporter (HXT) gene instead of the native HXTs[37]. We found that on high glucose (10 $gL^{-1}$), a fraction of cells (3.06% ± 0.96%; mean ± SEM, 4 independent biological experiments, n=966 cells) remained unbudded during the ≥ 40-hour observation period (Figure 1a), in contrast to wild type, where all cells budded (n=789 cells). To test if these non-dividing cells are viable, we assessed their capacity to produce biomass. We found that the non-dividing cells increased in volume nearly two-fold over time (Figure 1b), and also almost tripled their GFP content when GFP was expressed via a constitutive promoter (Figure 1c; Extended Data Figure 1a), demonstrating their viability. Using the localization of the transcriptional inhibitor Whi5 as a reporter of cell cycle phase, we found that all non-dividing cells were arrested in G1, and thus, had not undergone Start (Extended Data Figure 1b).

To test if the G1-arrested cells had lower glucose uptake rate compared to coexisting dividing cells, we provided the cells with a ≈20-min pulse of the fluorescent glucose analogue 2-[N-(7-nitrobenz-2-oxa-

1,3-diazol-4-yl) amino]-2-deoxy-d-glucose (2-NBDG), which is not metabolized further in glycolysis after its uptake and phosphorylation[38]. We found that the G1-arrested cells displayed significantly lower increase in 2-NBDG fluorescence in comparison to the dividing cells (Figures 1d and 1e), indicating that they indeed have a lower glucose uptake rate. Consistently, we found that feeding wild type cells in the microfluidics device with steady, very low concentrations of glucose, which at around 0.025 $gL^{-1}$ becomes limiting for glucose uptake[39], led to up to ≈80% of G1-arrested cells in the population (Extended Data Figure 1d). These findings indicate that cells with low glycolytic flux are able to produce biomass and increase in size, but fail to pass Start.

**High glycolytic flux enables Start by allowing for fast protein production**

To test if the low metabolic flux was indeed limiting for Start, we constructed a strain in which glycolytic flux could be orthogonally controlled in an otherwise unaltered nutrient environment. Specifically, because in single-HXT strains the glucose uptake rate directly correlates with Hxt expression levels[40], we introduced the glucose transporter gene HXT1 under the control of a tetracycline inducible promoter in a strain lacking all native glucose transporters[41]. In the absence of tetracycline, we found that leaky Hxt1 expression (Extended Data Figure 1e) led to the coexistence of dividing and non-dividing cells (≈8% of 220 cells, observed for over 16 h), similarly to what we observed in the other low-flux strain (TM6*). Whi5-GFP localization demonstrated that also these non-dividing cells were arrested in G1 (Extended Data Figure 1b). Upon induction of Hxt1 expression, 94.9% of the G1-arrested cells passed Start (Figure 1f). Start occurred only after the increase in Hxt1 levels, as shown with an Hxt1-GFP fusion (Figure 1f inset). Similarly, we found that the low-flux TM6* G1-arrested cells could also pass Start in response to increased glycolytic flux, accomplished by switching the feed from glucose to maltose (Extended Data Figures 1f and 1g). Note that maltose also fuels glycolysis, but in the TM6* strain with a higher rate compared to glucose (Extended Data Figure 1f), since it is taken up via HXT-independent transport[42]. These experiments show that the level of glycolytic flux can be rate-limiting for Start.

We hypothesized that the increase in glycolytic flux enables Start by allowing for faster protein production. To test this, we first determined the rate of protein production in the low-flux TM6* G1-arrested cells and in the coexisting high-flux dividing cells. Specifically, we determined the rate of yEGFP accumulation in newly born cells (Figure 1g – upper panel), when yEGFP was expressed from a constitutive Tet-On promoter[43]. We found that following cell birth, the low-flux G1-arrested cells had significantly lower rates of protein production compared to cells that managed to pass Start (Figure 1g – lower panel). When we shifted the cells from glucose to maltose, which leads to substantial increase in glycolytic flux (Extended Data Figure 1f), we found that the G1-arrested cells displayed a pulse in the

rate of protein production before passage through Start (Extended Data Figure 1h). To obtain the time evolution of single-cell GFP production rates, we first smoothed the total GFP abundance time series of each cell by fitting a Gaussian process model, and then calculated the derivative of the Gaussian process posterior function (see Methods). We observed the same pulse response when we shifted wild type cells arrested in G1 on low (0.01 $gL^{-1}$) glucose, to high (20 $gL^{-1}$) glucose (Figure 1h). We found that the increase in the rate of protein production upon increase of glycolytic flux was necessary for Start, since addition of 100 $\mu gL^{-1}$ cycloheximide (60 min after the switch to high glucose) prevented cells from undergoing Start (Figures 1h and 1i). Thus, an induced increase in glycolytic flux leads to a pulse in the rate of protein production, which is required for passage through Start.

**Cells in steady nutrient conditions exhibit pulses in protein production in synchrony with metabolic oscillations**

Next, we asked whether the intrinsic dynamics of metabolism during the cell cycle[28,29] are related to changes in the overall rate of protein production. First, we confirmed that also in wild type cells growing at steady-state conditions, there is an increase in glucose uptake rate during G1 (Figures 2a-2c). Then, to test the connection between metabolic and protein production dynamics, we measured in single cells the production rate of sfGFP (driven by the TEF1 promoter) while concomitantly monitoring NAD(P)H autofluorescence[29,44], which has been previously used to report glycolytic flux dynamics in yeast[45] (Extended Data Figures 2a and 2b). To define the timing of Start, we recorded the localization of Whi5-mCherry. We found that during unperturbed growth, cells displayed pulses in protein production rate during G1, which were in phase with the NAD(P)H oscillations, and coincided with Start (Figures 2d, 2e, and Extended Data Figures 2c-2e).

To test if the dynamic changes of metabolism were necessary for the pulses in the protein production rate, we perturbed glycolytic flux during G1 by temporarily adding to the 20 $gL^{-1}$ glucose medium, 2 $gL^{-1}$ of the non-metabolizable glucose analogue 2-Deoxy-D-glucose (2-DG), which is taken up, phosphorylated by hexokinase, but not metabolized further into glycolysis[46]. We found that the addition of 2-DG prevented the increase in NAD(P)H levels during G1 (Figure 2f), dramatically reduced the rate of protein production (Figure 2g), and prevented cells from undergoing Start (Figure 2h). In turn, removal of 2-DG led to increase in NAD(P)H levels, recovery of the protein production rate, and subsequent passage through Start (Figures 2f-2h). Thus, under steady conditions, cells exhibit pulses in the rate of protein production, which are in synchrony with metabolic oscillations and are essential for Start.

**The pulses in the rate of protein production follow the metabolic, rather than the cell size dynamics**

Next, we checked whether the dynamics of the protein production rate follow the dynamics of cell size during G1, as previously conjectured[13,16]. Here, while the protein production rate scaled globally with cell size (mean cell size during G1 versus mean production rate during G1; Spearman r: 0.596, p-value <0.0001, n=50 cells), we found that the dynamic changes in the rate of protein production were not accompanied by respective changes in cell size during G1 in single cells. Specifically, while the rate of protein production displayed a pulse-like behaviour, cell size increased continuously during G1 almost until the bud emerged (Figure 3a, Extended Data Figures 3a and 3b). At the peak of the pulse, the increase in the rate of protein production during G1 was on average nearly 1.5 to 2-fold higher than the respective increase in cell size (Figure 3b, Extended Data Figure 3b). These findings indicate that the dynamics of protein production rate are not coupled to those of cell size during the cell cycle. Remarkably, we observed the uncoupling between protein production rate and cell size dynamics in both small and large cells (Figures 3c-3e), as well as in cells that occasionally displayed more than one pulse in protein production during a longer-than-usual G1, where protein production rate also correlated with the intrinsic metabolic dynamics, but not with cell size dynamics (Figure 3f, Extended Data Figures 3c and 3d). Collectively, these findings demonstrate that, contrary to common assumptions, protein production and cell size dynamics scale differently during G1.

**Cln3 concentration increases severalfold around Start as a result of the pulse in protein production**

Given the differential scaling between protein production rate and cell size dynamics, we hypothesized that the concentration of Cln3 could increase during G1, in case Cln3 production has a similar profile as the TEF1-driven sfGFP production. In fact, TEF1 is a growth gene and transcription of CLN3 along with growth and ribosomal genes has been shown to be metabolically-induced[33]. However, unlike sfGFP alone, Cln3-sfGFP cannot be detected, likely due to fast degradation of the protein fusion, which does not leave sufficient time for fluorophore maturation after translation (Extended Data Figures 4a and 4b). To overcome the technical limitation of measuring the *in vivo* production dynamics of the wild type Cln3, we generated a genomic fusion of Cln3 and sfGFP at the endogenous CLN3 locus, with a sequence encoding for a 2A self-cleaving peptide from the porcine teschovirus-1 added in-between the two genes (Figure 4a). Since 2A peptides undergo non-enzymatic self-cleavage co-translationally, proteins linked by 2A peptides are synthesized stoichiometrically, but exist after translation as two unlinked proteins[47]. Thus, using a genomic Cln3-2A-sfGFP fusion, we could uncouple the post-translational fate of Cln3 and sfGFP, and despite the fast Cln3 degradation, sfGFP remained undegraded and detectable (Figure 4b). In this way, by measuring the dynamic production rate of sfGFP, we could estimate that of Cln3.

To confirm that Cln3-2A-sfGFP reports Cln3 production, we mutated the uORF at position −315 in the 5' mRNA leader of CLN3. Consistent with the function of the uORF to suppress Cln3 translation in slow growth conditions[15], we observed a ≈50% increase in sfGFP produced via the Cln3-2A-sfGFP fusion in the A-315T/CLN3 strain compared to the wild type under such conditions (Extended Data Figure 4c). Moreover, we found a good agreement between Cln3 levels determined via the Cln3-2A-sfGFP fusion in single cells, and recently reported[27] bulk Cln3 measurements across different growth rates (Extended Data Figure 4d). Thus, Cln3-2A-sfGFP expressed from the endogenous CLN3 promoter can be used to determine Cln3 levels in single cells.

By determining the rate of sfGFP accumulation over time, we found that sfGFP from the Cln3-2A-sfGFP fusion was also produced in pulses (Figure 4c, Extended Data Figures 4e-4i), similarly to sfGFP produced by the TEF1 promoter (Figure 2d). We observed pulses with severalfold increase in the rate of Cln3 production (Figure 4c, Extended Data Figures 4h and 4i), again in contrast to the comparably small increase in cell size (Extended Data Figures 4h and 4i). Taking into consideration that Cln3 abundance is nearly proportional to Cln3 production rate (see Note in Methods and Extended Data Figure 8), and employing the measured dynamic changes in cell size and sfGFP production rate, we calculated a severalfold increase in the concentration of Cln3 during G1 (Figure 4d). To confirm that the concentration of Cln3 increases during G1, we isolated small, unbudded G1 cells by centrifugal elutriation, and performed targeted proteomics to measure Cln3 abundance during G1 progression. In parallel, we determined cell size. Consistent with our single cell data, also here, we observed a pulse in Cln3 abundance during G1 without an equivalent increase in cell size (Figure 4e), which together resulted in an increase in Cln3 concentration (Figure 4f) before cell cycle commitment. Altogether, these results demonstrate that the pulse in the rate of Cln3 production, and its mismatch with cell size dynamics, lead to increase in the concentration of Cln3 in G1.

**The pulses in Cln3 concentration are responsible for Start**

To understand how this increase in Cln3 concentration contributes to Start, we measured also the concentration dynamics of its target, Whi5. Here, we detected only a small or no change in Whi5 concentration during G1 by either microscopy or targeted proteomics measurements (Figure 5a, Extended Data Figures 5a and 5b). In contrast, Cln3 concentration not only increased severalfold during G1 (Figures 4d and 4f), but we found that the pulse in Cln3 production rate coincided with the time of Start (Figure 5b). Furthermore, we determined the dynamics of Whi5 localization, along with the dynamics of Cln3 and Cln2 production. We found that the increase in Cln3 production rate coincided with the onset of Whi5 exit from the nucleus (Figure 5c), with the increase in Cln2 production following closely afterwards, right before the complete translocation of Whi5 to the cytoplasm (Figure 5d). Thus,

the ordered occurrence of the pulse in Cln3 production, the onset of Whi5 translocation to the cytoplasm, and the activation of Cln2 production, suggests that in the absence of major changes in Whi5 concentration (Figure 5a, Extended Data Figure 5b), the increase in Cln3 concentration is the primary cause for Start.

To confirm that the increase in Cln3 levels is the primary determinant of the timing of Start, we decoupled the dynamics of Cln3 levels from the overall dynamics of protein production. To do this, we allowed cells to undergo regular pulses in protein production rate, but dynamically prevented Cln3 levels from increasing, by enhancing the degradation rate of Cln3 via the auxin-inducible degron (AID)[51,52] (Figure 5e). In parallel, we monitored Whi5-mCherry localization dynamics to define Start, and estimated the overall protein production dynamics by measuring sfGFP expressed via the TEF1 promoter. Here, we found that preventing Cln3 levels from increasing normally during the pulse in protein production rate in wild type cells that were previously undergoing unperturbed cell division cycles, and thus, cells that were adjusted to having normal Cln3 dynamics, led to an up to ≈ 13-fold increase in the median duration of pre-Start G1 (Figures 5f and 5g, Extended Data Figure 5c). Interestingly, despite the remarkably long G1 duration, when Start occurred, it also here did so during a pulse in protein production, which then had a nearly 2-fold higher peak rate compared to the normal pulses (Figure 5f, Extended Data Figure 5d). These findings demonstrate that the dynamics of Cln3 constitute the primary determinant of the timing of Start.

**The differential scaling between Cln3 production rate and cell size dynamics explains Start across different nutrient conditions and cell age**

As Start control has been so far almost exclusively studied in daughter cells, we then asked whether the differential scaling between Cln3 production rate and cell size is responsible for Start also in mothers. Indeed, we found that mother cells increased in cell size only marginally between cytokinesis and Start, and Whi5 concentration remained constant during that time (Figure 6a). Furthermore, similarly to daughters, mother cells displayed also a pulse in Cln3 production that coincided with Start (Figure 6b), indicating that the same mechanism for Start applies also to mothers. Remarkably, the pulse in Cln3 production was initiated already before cytokinesis and peaked shortly after the onset of G1 phase (Figure 6b), possibly explaining the shorter G1 duration in mothers.

If the differential scaling between Cln3 production rate and cell size dynamics is the primary cause of Start, we argued that apart from daughters and mothers on a certain nutrient, this mechanism has to explain Start also across different growth conditions. While so far we focused on cells growing on glucose, metabolic oscillations in synchrony with the cell cycle have been observed across nutrient environments[29]. Therefore, we measured the metabolic, biosynthetic, and cell cycle activity also under

different nutrient conditions, where doubling times ranged from ≈1.5 to more than 5.5 hours. Also here, we observed small or no change in Whi5 concentration during G1 (Extended Data Figures 6a-6c), but we found that cells exhibited pulses in the rate of protein production in synchrony with metabolic oscillations (Extended Data Figures 6d and 6e), without corresponding increase in cell size (Extended Data Figures 6f and 6g). Also under these growth conditions, Start occurred during the Cln3 pulse (Figures 6c, 6d, Extended Data Figures 7a-7d). Thus, these data indicate that Cln3 concentration dynamics determine the timing of Start across different nutrient conditions.

Finally, because during replicative ageing yeast cells undergo dramatic changes in their physiology, even if nutrient conditions are retained constant[53], we asked whether the here identified mechanism is responsible for Start also in replicatively aged cells. To test this, we used our microfluidic device to obtain replicatively aged cells, and monitored Cln3 and Whi5 dynamics along with cell cycle progression. Also in this case, we observed only minor changes in Whi5 concentration, and Start occurred during pronounced pulses in Cln3 production (Figure 6e). These findings indicate that Cln3 dynamics are responsible for Start independently of cell age.

## DISCUSSION

Using single-cell time-lapse fluorescence microscopy combined with meticulous image and data analysis, we measured metabolic, biosynthetic, and cell cycle activity concomitantly, in unperturbed *S. cerevisiae* cells growing at various steady and dynamic nutrient environments. We show that the overall rate of protein production increases considerably more than cell size during G1, and thus, these two fundamental physiological parameters do not scale with each other in the course of the cell cycle. Using a viral-based bicistronic construct and targeted proteomics, we show that Cln3 is produced in pulses, which follow the intrinsic metabolic dynamics, and which lead to increase in Cln3 production rate that is proportionally larger than the respective increase of cell size during G1. This differential scaling between Cln3 production rate and cell size dynamics leads to a severalfold increase in the concentration of Cln3, causing cell cycle Start (Figure 6f). Collectively, we have identified a cause of Start that is universal for daughter and mother cells, as well as across growth conditions.

Our finding that protein production rate displays a pulse-like behaviour contradicts early population- and single-cell level measurements, which suggested an exponentially increasing rate of protein production during the cell cycle[17,18]. However, cell cycle dependent trends can be easily masked in population-level experiments, and on the other hand, dynamic trends in single-cell approaches are particularly prone to molecular and technical noise. In accordance with our results, recent single-cell measurements showed a marked slowdown in the accumulation rate of a constitutively expressed fluorescent protein during the G1-S transition[19], indicative of the pulsing behaviour of protein

production rate that we describe here. Moreover, it was proposed that protein production decreases as a result of induced polarization of the actin cytoskeleton[22]. Thus, our finding that the rate of protein production decreases after Start following its pulse, is consistent with the fact that in late G1 there is polarization of the actin cytoskeleton[54]. Furthermore, the increase in cell density that has been reported to occur around Start[55] could be explained by our finding that the disproportional increase of protein production rate with respect to cell size is highest around this period.

The dynamics of Cln3 during G1 have remained elusive for almost two decades. Resolving the technical hurdle of measuring the production rate of wild type Cln3 in single cells during the cell cycle utilizing a viral-based bicistronic construct, and combining this with parallel cell size measurements, we found that Cln3 concentration increases during G1. We confirmed the increase in Cln3 concentration during G1 using targeted proteomics, thereby also confirming the assumption which underlies the experiments with the bicistronic construct, i.e. that any potential temporal variations in the post-translational regulation of Cln3 abundance (e.g. dynamics in Cln3 degradation) during G1 do not play a major role. In contrast to previous attempts to quantify Cln3 levels in single cells[13], we did not rely on hyper-stabilized mutant versions of the Cln3 protein, whose dynamics are expected to be less pronounced in comparison to those of wild type Cln3. Moreover, to account for inherent cell-to-cell variability, we examined cell-cycle related Cln3 dynamics either in time-traces of individual cells, or in averaged single-cell data aligned at the moment of Start, something which was not done earlier.

While it was recently proposed that the timing of Start is determined by the dilution of Whi5[13], accumulating evidence from more recent studies contradicts this model. In accordance with our findings, Dorsey *et al.* did not observe any dilution of Whi5 in different genetic backgrounds and nutrient conditions, attributing reported changes in Whi5 concentration to photobleaching[26]. Moreover, although the inhibitor dilution model suggests that the increase in cell size during G1 determines the timing of Start, it was recently shown that there is no significant correlation between cell size and the rate of cell division[27], and thus, it is unclear how this model applies to different growth conditions. Finally, even assuming cell size-dependent changes in Whi5 concentration during G1, the Whi5-dilution model would fall short of robustly explaining the timing Start in mother yeast cells, given that mother G1 is associated with very small changes in cell size (Figure 6a, Extended Data Figures 6b and 6c), while G1 duration can remarkably vary (Figure 6d).

In contrast, as we show here, the differential scaling between protein production rate and cell size can constitute a universal mechanism for Start, applying to both daughter and mother cells, as well as across different growth conditions. We show that the increase in Cln3 concentration is the primary trigger for the G1/S transition. Still, other mechanisms might act in parallel to fine-tune the timing of

Start. For example, as cells proceed through G1, the accumulation of the SBF-component Swi4[26] downstream of Cln3, or the chaperone-mediated release of ER-retained Cln3[24,56] can potentially further increase the probability of Start. It is possible that under specific growth conditions, changes in Whi5 levels[13] may also contribute to Start.

Furthermore, our findings show that the dynamics of protein production rate follow the intrinsic metabolic dynamics, suggesting a connection between the two. Also, we show that high metabolic flux enables the attainment of high overall protein, and by extension, Cln3 production rates. In fact, it was hypothesized almost a decade ago that a metabolic burst during G1 could boost translation, and thereby Cln3 production[57], although experimental evidence was missing. Nevertheless, the truth is possibly more complex than simply metabolic dynamics governing protein production rates. In yeast and higher eukaryotes, there are feedback interactions between metabolism and protein production[58,59], and how exactly these processes influence each other in the course of the cell cycle remains to be revealed.

Early work had suggested that Start relies on the attainment of a critical protein production rate[60] which is necessary for the accumulation of specific activating proteins, and it was conjectured already by Unger and Hartwell that the unifying signal linking physiological status to the cell cycle decisions is the rate of protein production[34]. Our results demonstrate that this view was correct. Crucially, however, we additionally show that increased protein production rates control cell cycle Start due to the differential scaling between protein production rate and cell size during G1. Moreover, a sufficiently strong metabolic flux is required for the attainment of high protein production rates, suggesting that cells assess both their metabolic state and biosynthetic capacity before committing to entering the cell division cycle.

Due to the high degree of conservation of core metabolism[61] and the G1-control network across eukaryotes[62], we envision that similar principles for cell cycle commitment may apply also to higher eukaryotes.

**ACKNOWLEDGEMENTS**

The authors thank Benjamin Tu for critical comments on an early version of the manuscript; Zheng Zhang for advice on microscopy; Christoffer Åberg for discussions on model-based analysis of microscopy data, and the Ida van der Klei lab for the kind provision of the pSNA10 plasmid. Financial support was provided by the EU ITN project ISOLATE (grant agreement 289995).

**AUTHOR CONTRIBUTIONS**

A.L. and M.H. conceived the study. A.L., M.H. and A.M.-A. designed the study. A.L. constructed the strains, performed the experiments, and analysed the data. D.H.E.W.H. performed preliminary experiments and contributed conceptually. H.T. participated in strain construction and culture sampling for targeted proteomics. A.M.-A. performed the smoothing and derivative estimation for the single-cell time-lapse data. P.G. performed and analysed the verification experiments with confocal microscopy. A.S. and K.B. performed targeted proteomics and analysed the data. A.P. participated in strain construction, metabolite measurements during batch cultivation, and did preliminary data analysis. M.R. performed the elutriation and participated in culture sampling for targeted proteomics and respective data analysis. J.H. prepared protein samples for mass spectrometry. G.H. performed the model-based analysis of the metabolite data for estimation of cellular physiology. M.E. participated in strain construction. A.L. and M.H. wrote the manuscript with input from A.M.-A.. M.H. and A.M.-A. supervised the study.

**DECLARATION OF INTERESTS**

The authors declare no competing interests.

.

## FIGURE CAPTIONS

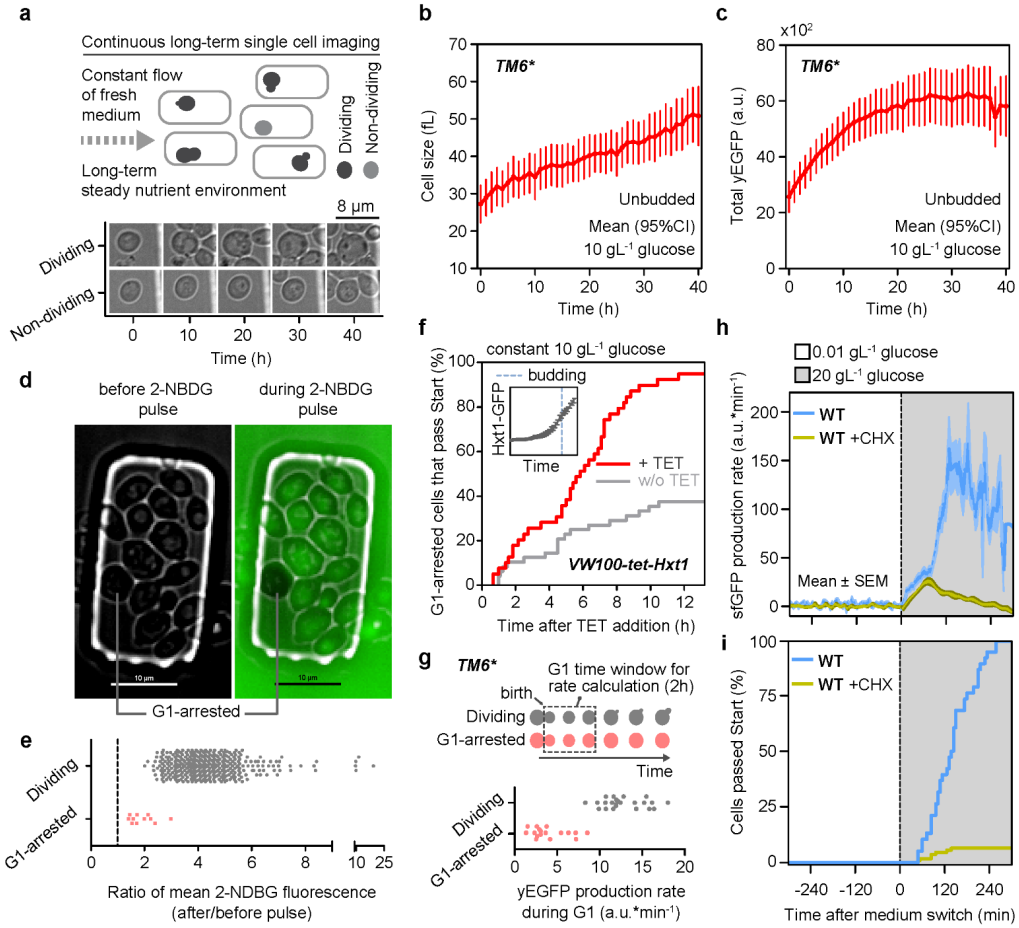


**Figure 1** | **High glycolytic flux enables Start by allowing for fast protein production.** (**a**) Above: Schematic of microfluidics-based experimental setup. Cells are trapped underneath PDMS pads and continuously fed with fresh medium. Below: Time-lapse images of coexisting dividing and non-dividing cells. Experiment repeated independently 4 times with similar results. (**b**) Cell size (n=18 cells) and (**c**) total yEGFP content (n=14 cells) of non-dividing cells over time. yEGFP expressed via Tet-ON promoter[43] (300 ng*mL$^{-1}$ TET). (**d**) Merged phase-contrast and fluorescent images of TM6* cells (10 gL$^{-1}$ glucose) before and during pulse with 0.01 gL$^{-1}$ glucose supplemented with 60 µM 2-NBDG. Experiment performed once with multiple imaging positions. (**e**) Ratio of mean cellular 2-NBDG fluorescence after and before the pulse in G1-arrested (cells that remained unbudded for the whole observation period (>24 hours); n=11) and dividing cells (rest of the cells; n=373) (Mann Whitney test p-value <0.0001). Among dividing cells, a significant negative correlation between G1 duration and G1 glucose uptake rate was observed (Extended Data Figure 1c). (**f**) Percentage of G1-arrested cells (n=39 cells) that pass Start (as indicated by bud emergence) in response to addition of 50 ng*mL$^{-1}$ TET. Control (n=48 cells): no TET (log-rank (Mantel-Cox) test p-value <0.001). Inset: Hxt1-GFP levels in response to TET addition in cells (n=25 cells) aligned for the moment of bud emergence. (**g**) Average protein (yeGFP) production rate during G1 in dividing

(n=23 cells) and G1-arrested (n=17 cells) TM6* cells. Gain in total yeGFP during the first 2 hours after birth was determined, and this value was divided by 120 to obtain per-minute yeGFP production rate. (**h**) Dynamics of protein (sfGFP) production rate in G1-arrested wild type cells (n=36 cells) and (**i**) respective fraction of cells that pass Start in response to increase in glycolytic flux achieved by switching the feed from 0.01 to 20 $gL^{-1}$ glucose. Control: 60 min after the switch to 20 $gL^{-1}$ glucose, 100 $ng*mL^{-1}$ CHX added (n=29 and 107 cells for (**h**) and (**i**) respectively). For (**i**), log-rank (Mantel-Cox) test p-value <0.001. sfGFP expressed via the TEF1 promoter. Source data for **b**-**c** and **e**-**i** are provided in Source Data Figure 1.

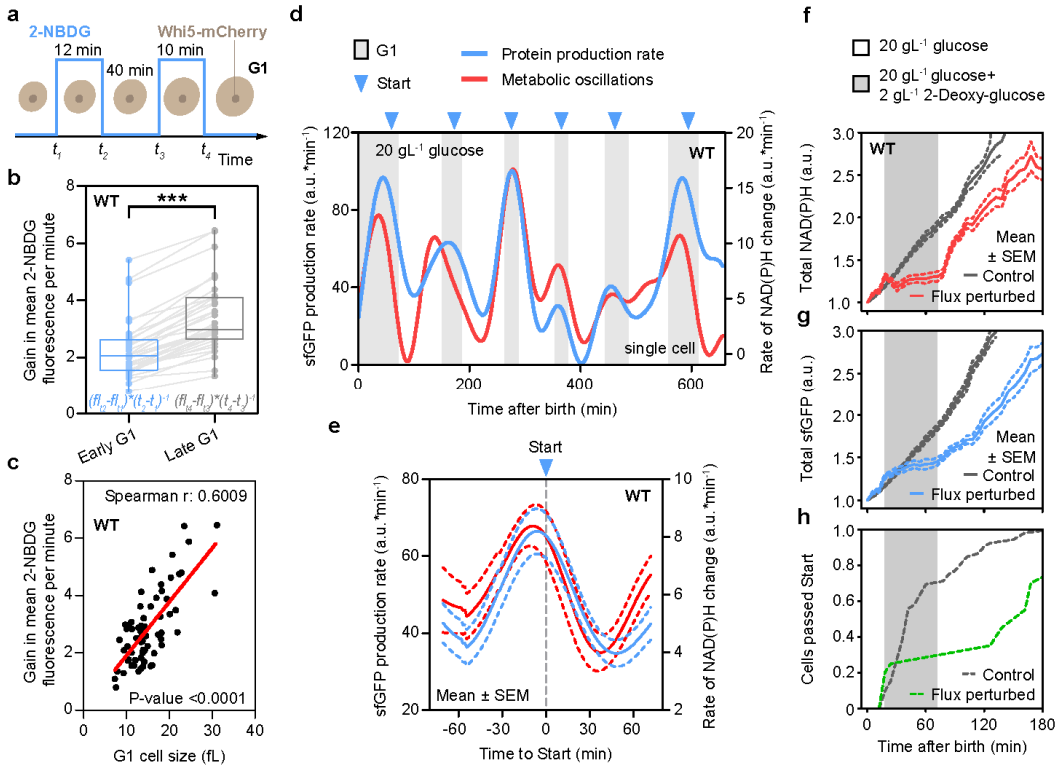


**Figure 2** | **At steady conditions, cells display pulses in the rate of protein production which are in synchrony with metabolic oscillations and are required for Start.** (**a**) Schematic representation of experiment for assessing glucose uptake rate dynamics during G1. G1 cells growing in 0.05 $gL^{-1}$ glucose were subjected to two subsequent pulses of 0.05 $gL^{-1}$ glucose plus 60 µM 2-NBDG. Whi5-mCherry localization was monitored in parallel, to detect cells that were in G1 and had not passed Start during either of the two pulses. In this way, the difference in glucose uptake rate between an early and a later G1 stage could be determined for the same single cell. (**b**) 2-NBDG uptake in the same individual cells (n=33 cells) during the first and the second pulse (***: Wilcoxon signed rank test, p-value <0.0001). 2-NBDG uptake was estimated by calculating the gain in fluorescence per pulse ($fl_{tn+1}$ - $fl_{tn}$) for each cell, and dividing it by the duration of each pulse ($t_{n+1}$ - $t_n$). Boxplot: box extends from the 25$^{th}$ to 75$^{th}$ percentiles and whiskers down to the min and up to the max value. (**c**) 2-NBDG uptake rate as a function of G1 cell size (n=66 cells). (**d**) Dynamics of sfGFP production rate and rate of NAD(P)H change in a single wild type cell at steady glucose (20 $gL^{-1}$) environment. (**e**) Dynamics of sfGFP production rate and rate of NAD(P)H change

in cells aligned for Start (n=16 cell cycles). Dynamics of (**f**) total NAD(P)H and total (**g**) sfGFP in response to addition and removal of 2-DG (2 $gL^{-1}$) in wild type cells (n=20 cells) growing in steady glucose (20 $gL^{-1}$) environment. Note that due to the abrupt effect of 2-DG on NAD(P)H and sfGFP dynamics, smoothing splines required for estimation of rates cannot reliably capture the timing of the changes, and thus, the respective NAD(P)H and sfGFP abundances are presented directly. (**h**) Cumulative distribution of cells (from **f**-**g**) passing Start. In the control experiments (grey lines; n=52 cells), no 2-DG was added. Source data for **b**-**h** are provided in Source Data Figure 2.

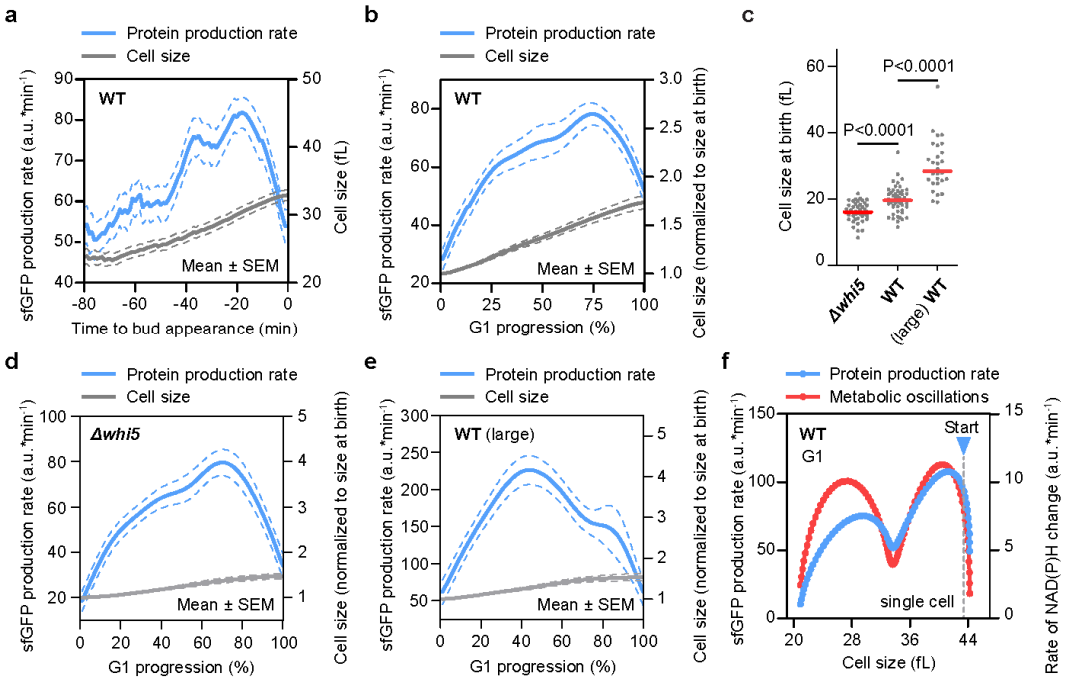


**Figure 3** | **Cells display pulses in the rate of protein production during G1 which and are not accompanied by respective changes in cell size.** (**a**) sfGFP production rate and respective cell size dynamics in wild type daughter cells aligned for the moment of bud appearance (n=50 cells). (**b**) sfGFP production rate and respective cell size dynamics for normalized G1 progression in the same cells as in (**a**). (**c**) Cell size at birth in cells of the *Δwhi5* cell size mutant (n=44 cells), in wild type cells born by young mothers (WT, n=50 cells), and in wild type cells born by replicatively aged mothers ((large) WT, n=29 cells). Indicated p-values from Mann Whitney tests. Vertical lines denote the median. (**d**) sfGFP production rate and respective cell size dynamics for normalized G1 duration in *Δwhi5* mutants (n=44 cells) and (**e**) large wild type cells born by replicatively aged mothers (n=29 cells). (**f**) Dynamics of sfGFP production rate and rate of NAD(P)H change during G1 in a single wild type cell as a function of cell size. In all cases, sfGFP expression was driven by the TEF1 promoter. Source data for Figure 3 are provided in Source Data Figure 3.

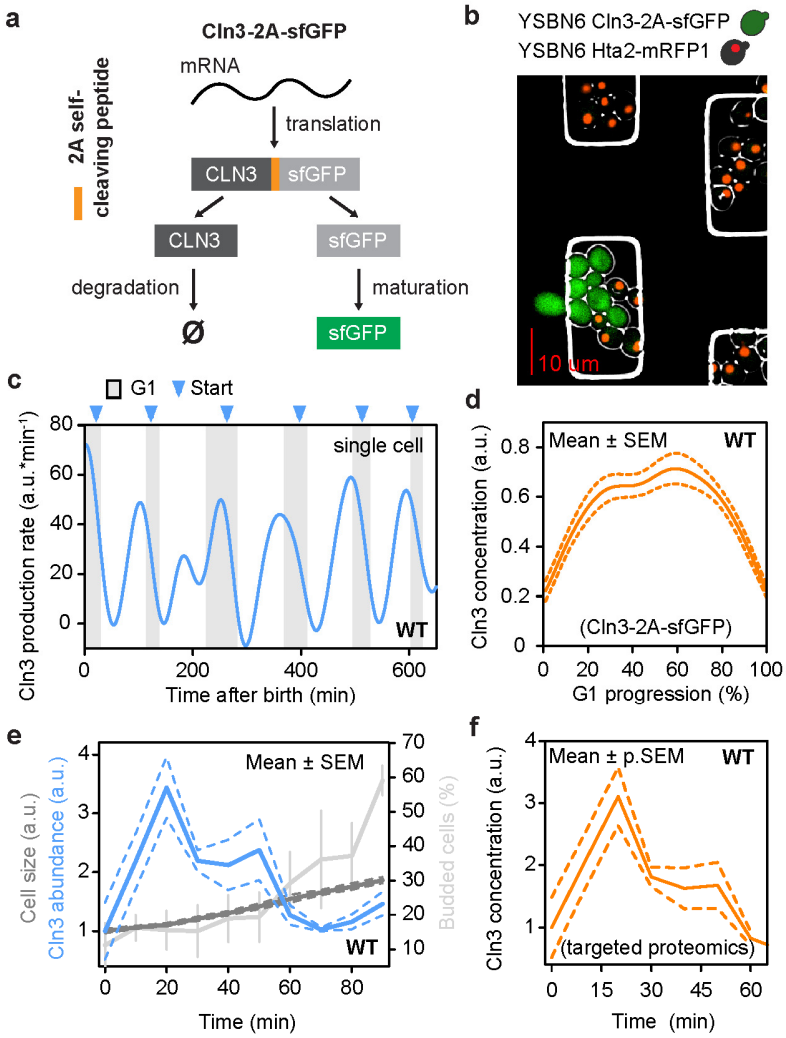


**Figure 4** | **Cln3 concentration changes severalfold during the cell cycle as a result of the pulse in its production rate, and the differential scaling between the latter and cell size dynamics.** (**a**) Incorporation of a viral self-cleaving peptide between Cln3 and sfGFP decouples the post-translational fate of Cln3 and sfGFP, allowing sfGFP to mature and report on Cln3 production rate. (**b**) Merged phase contrast and fluorescent (GFP and RFP channels) images of Cln3-2A-sfGFP wildtype cells mixed with wild type Hta2-mRFP1 cells as a control for cell autofluorescence at the GFP channel. Experiment was performed 3 times with similar results. (**c**) Dynamics of sfGFP production rate from the Cln3-2A-sfGFP fusion construct in a single cell. (**d**) Cln3 concentration dynamics in wild type daughter cells (n=41 cells) during normalized G1 progression. Since Cln3 is mainly nuclear[13,48] and because the volume of the nucleus scales proportionally to cell volume[49,50], changes in the nuclear volume reflect changes in the measured cellular volume. Therefore, the concentration of Cln3 can be approximated by dividing its abundance (extracted from its production rate (see Methods)) with the cell volume. In (**a**-**d**), cells grew in a steady glucose (20 $gL^{-1}$) environment and Cln3 in fusion with the 2A-sfGFP construct was expressed from its endogenous locus. (**e**) Dynamics of Cln3 abundance identified by targeted proteomics, cell size, and budding index, in small, mostly unbudded G1 cells, which were isolated by centrifugal elutriation and released (t = 0) into

YPD (n=4 independent biological experiments). (**f**) Cln3 concentration during the early cell cycle estimated on the basis of the Cln3 abundance and cell size dynamics in (**e**). Error bars show propagated SEM. Cln3 and cell size data in (**e**) and (**f**) are normalized to t = 0. Source data for **c**-**f** are provided in Source Data Figure 4.

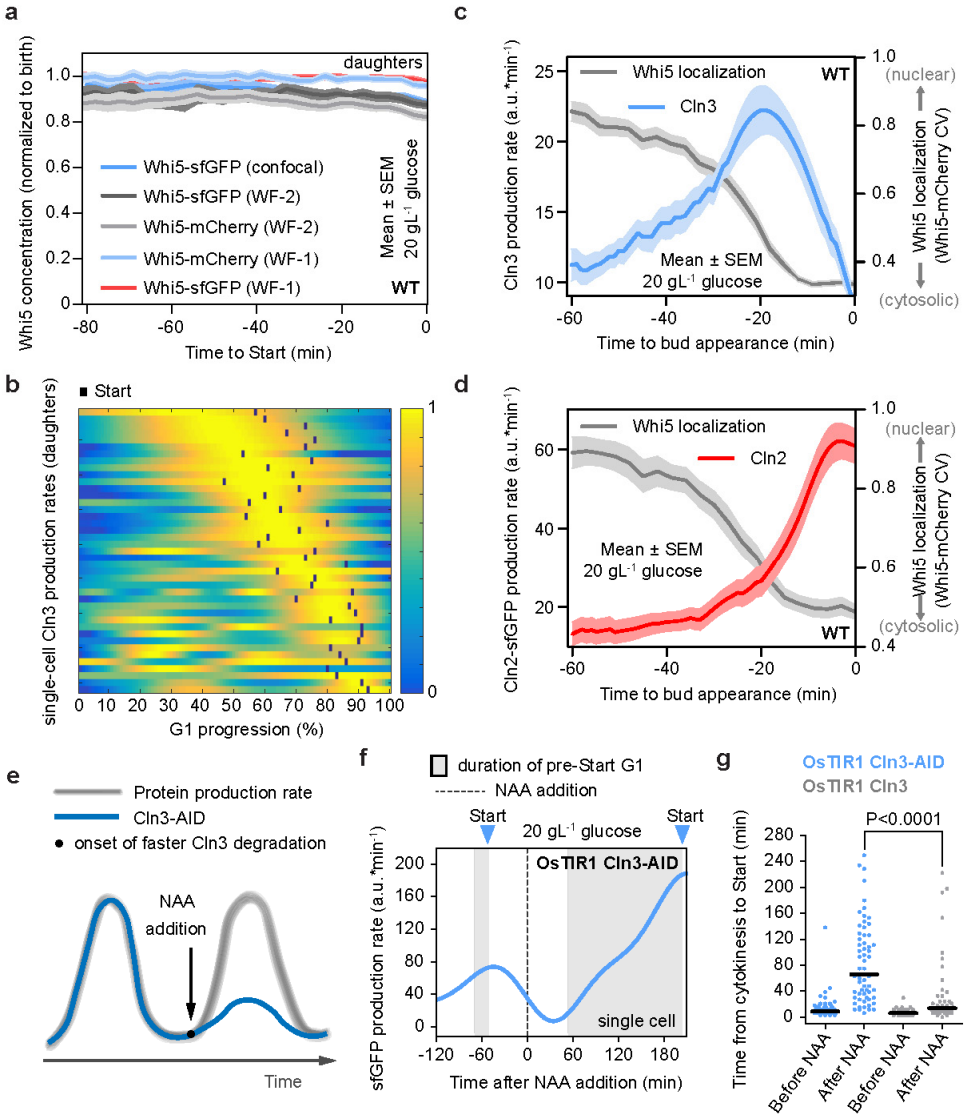


**Figure 5** | **The Cln3 pulses determine the timing of Start.** (**a**) Whi5 concentration in daughter cells, normalized for concentration at birth and aligned for the moment of Start. For widefield experiments, n=101 and 50 cells for Whi5-sfGFP, and 52 and 50 cells for Whi5-mCherry, for WF-1 and WF-2, respectively (WF-1: mean cell fluorescence; WF-2: integrated fluorescence over whole cell area divided by cell volume). For confocal, n=44 cells. (**b**) Heatmap showing the dynamics of the Cln3 production rate during G1 in single wild type daughter cells. For each cell, the Cln3 production rate time series was divided by the maximum value obtained during the corresponding observation window. The dark squares indicate the moment of Start in each cell. (**c**) Dynamics of Cln3 (n=41 cells) and (**d**) Cln2 (n=25 cells) production rate as a function of time and Whi5 localization in cells aligned for the moment of bud appearance. The production rate of Cln2 was estimated through a Cln2-sfGFP

fusion. (**e**) Schematic representation of induced Cln3 depletion in cells undergoing otherwise unperturbed cell division cycles. The synthetic auxin substitute naphthalene-acetic acid (NAA) is added to cells which express the plant F-box protein TIR1 and in which Cln3 is tagged with the auxin-inducible degron (AID). (**f**) Dynamics of sfGFP production rate in a single OsTIR1 Cln3-AID cell treated with NAA at the indicated time point. Pre-Start G1 is defined as the time of entry to G1 (cytokinesis) until the moment of Start. (**g**) Duration of pre-Start G1 before (n=56 and 44 cells) and after (n=61 and 46 cells) addition of 1mM NAA in OsTIR1 Cln3-AID and OsTIR1 Cln3 (control) cells. Indicated p-value from Mann Whitney test. Horizontal lines denote the median. In (**f**) and (**g**), sfGFP is expressed via the TEF1 promoter. In all cases, cells grew in a steady glucose (20 $gL^{-1}$) environment, and Start was determined via observation of Whi5-mCherry or Whi5-sfGFP localization. Source data for **a**-**d** and **f**-**g** are provided in Source Data Figure 5.

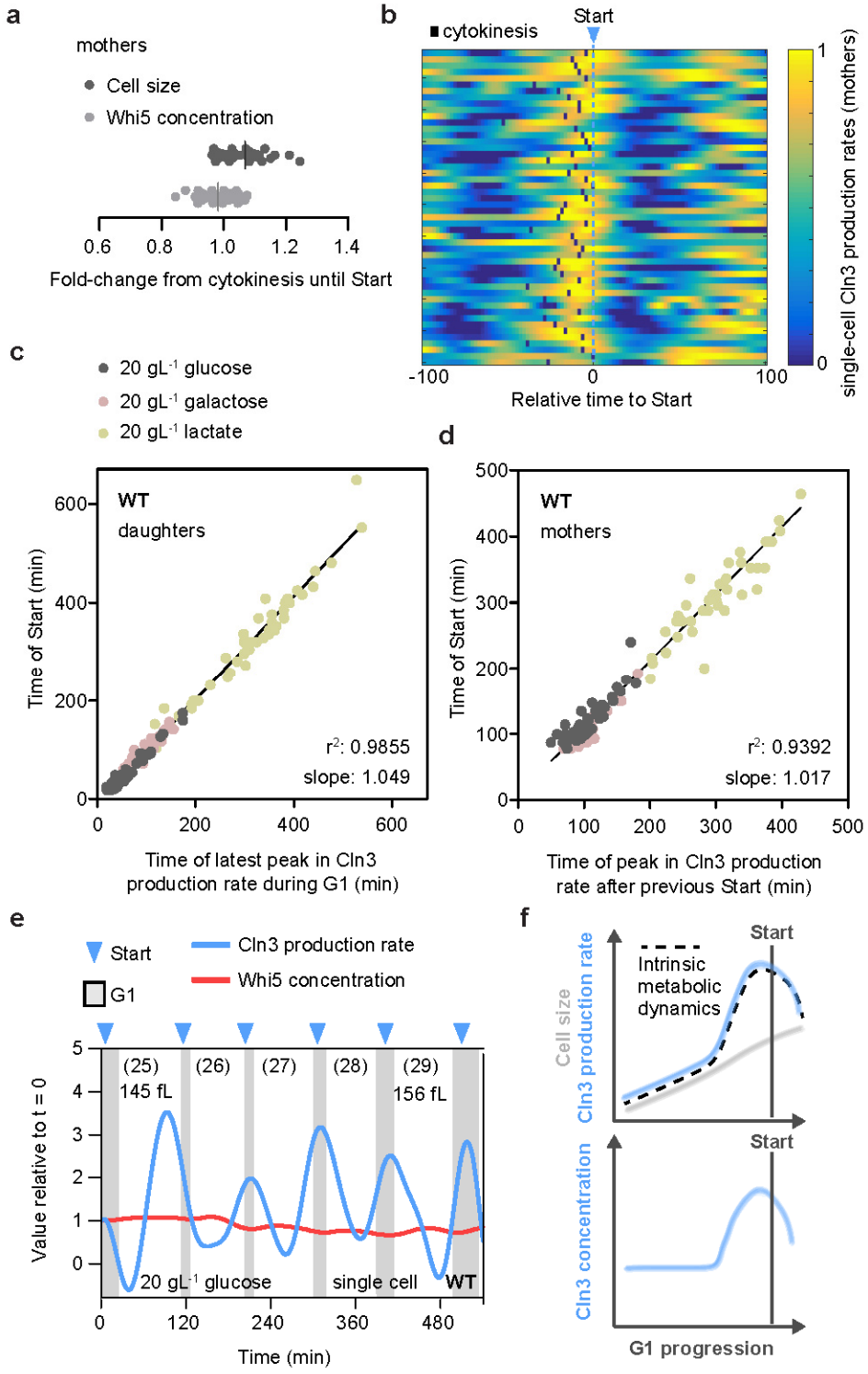


511

512 **Figure 6 | The differential scaling between Cln3 production pulses and cell size dynamics constitutes a**
513 **daughter/mother-, and growth-condition-independent cause of Start.** (**a**) Change in cell size and Whi5-sfGFP
514 concentration (integrated fluorescence over whole cell area divided by cell volume) between cytokinesis and
515 Start in mother cells (n=40 cells). The vertical lines denote the respective population average. (**b**) Heatmap

showing the dynamics of the Cln3 production rate in single wild type mother cells. Cells are aligned for Start (t = 0) and cytokinesis is indicated in each cell by a dark square. Data were normalized as in Figure 5b. (**c**) Time of latest peak in Cln3 production rate during G1 versus the moment of Start in individual daughter cells (n=120 cells, Spearman r: 0.9875), and (**d**) time of peak in Cln3 production rate after previous Start versus time between previous and next Start in individual mother cells (n=121 cells, Spearman r: 0.9415) growing on different carbon sources. (**e**) Cln3 production rate and Whi5 concentration dynamics in a single, wild-type, aged, large mother cell. Numbers in parentheses indicate the replicative age of the mother at each Start event. The cell size of the mother during the first and last displayed Start event is also shown. (**f**) Schematic representation of model for cell cycle commitment. The differential scaling between the rate of Cln3 production and cell size dynamics during G1 causes Start by leading to increase in Cln3 concentration. Source data for **a**-**e** are provided in Source Data Figure 6.

## REFERENCES


1. Johnson, A. & Skotheim, J. M. Start and the restriction point. *Curr. Opin. Cell Biol.* **25**, 717–23 (2013).

2. Nash, R., Tokiwa, G., Anand, S., Erickson, K. & Futcher, A. B. The WHI1+ gene of Saccharomyces cerevisiae tethers cell division to cell size and is a cyclin homolog. *EMBO J.* **7**, 4335–46 (1988).

3. Cross, F. R. DAF1, a mutant gene affecting size control, pheromone arrest, and cell cycle kinetics of Saccharomyces cerevisiae. *Mol. Cell. Biol.* **8**, 4675–84 (1988).

4. Tyers, M., Tokiwa, G. & Futcher, B. Comparison of the Saccharomyces cerevisiae G1 cyclins: Cln3 may be an upstream activator of Cln1, Cln2 and other cyclins. *EMBO J.* **12**, 1955–68 (1993).

5. Tyers, M., Tokiwa, G., Nash, R. & Futcher, B. The Cln3-Cdc28 kinase complex of S. cerevisiae is regulated by proteolysis and phosphorylation. *EMBO J.* **11**, 1773–84 (1992).

6. de Bruin, R. A. M., McDonald, W. H., Kalashnikova, T. I., Yates, J. & Wittenberg, C. Cln3 activates G1-specific transcription via phosphorylation of the SBF bound repressor Whi5. *Cell* **117**, 887–98 (2004).

7. Costanzo, M. *et al.* CDK activity antagonizes Whi5, an inhibitor of G1/S transcription in yeast. *Cell* **117**, 899–913 (2004).

8. Wang, H., Carey, L. B., Cai, Y., Wijnen, H. & Futcher, B. Recruitment of Cln3 cyclin to promoters controls cell cycle entry via histone deacetylase and other targets. *PLoS Biol.* **7**, e1000189 (2009).

9. Skotheim, J. M., Di Talia, S., Siggia, E. D. & Cross, F. R. Positive feedback of G1 cyclins ensures coherent cell cycle entry. *Nature* **454**, 291–6 (2008).

10. McInerny, C. J., Partridge, J. F., Mikesell, G. E., Creemer, D. P. & Breeden, L. L. A novel Mcm1-dependent element in the SWI4, CLN3, CDC6, and CDC47 promoters activates M/G1-specific transcription. *Genes Dev.* **11**, 1277–1288 (1997).

11. Zapata, J. *et al.* PP2ARts1 is a master regulator of pathways that control cell size. *J. Cell Biol.* **204**, 359–76 (2014).

12. Thorburn, R. R. *et al.* Aneuploid yeast strains exhibit defects in cell growth and passage through START. *Mol. Biol. Cell* **24**, 1274–1289 (2013).

13. Schmoller, K. M., Turner, J. J., Kõivomägi, M. & Skotheim, J. M. Dilution of the cell cycle inhibitor Whi5 controls budding-yeast cell size. *Nature* **526**, 268–72 (2015).

14. Jorgensen, P. & Tyers, M. How cells coordinate growth and division. *Curr. Biol.* **14**, R1014-27 (2004).

15. Polymenis, M. & Schmidt, E. V. Coupling of cell division to cell growth by translational control of the G1 cyclin CLN3 in yeast. *Genes Dev.* **11**, 2522–31 (1997).

16. Schmoller, K. M. & Skotheim, J. M. The Biosynthetic Basis of Cell Size Control. *Trends Cell Biol.* **25**, 793–802 (2015).

17. Elliott, S. G. & McLaughlin, C. S. Rate of macromolecular synthesis through the cell cycle of the yeast Saccharomyces cerevisiae. *Proc. Natl. Acad. Sci. U. S. A.* **75**, 4384–8 (1978).

18. Di Talia, S., Skotheim, J. M., Bean, J. M., Siggia, E. D. & Cross, F. R. The effects of molecular noise and size control on variability in the budding yeast cell cycle. *Nature* **448**, 947–51 (2007).

19. Cookson, N. A., Cookson, S. W., Tsimring, L. S. & Hasty, J. Cell cycle-dependent variations in protein concentration. *Nucleic Acids Res.* **38**, 2676–81 (2010).

20. Soifer, I., Robert, L. & Amir, A. Single-Cell Analysis of Growth in Budding Yeast and Bacteria Reveals a Common Size Regulation Strategy. *Curr. Biol.* **26**, 356–61 (2016).

21. Bryan, A. K., Engler, A., Gulati, A. & Manalis, S. R. Continuous and long-term volume measurements with a commercial Coulter counter. *PLoS One* **7**, e29866 (2012).

22. Goranov, A. I. *et al.* The rate of cell growth is governed by cell cycle stage. *Genes Dev.* **23**, 1408–22 (2009).

23. Ferrezuelo, F. *et al.* The critical size is set at a single-cell level by growth rate to attain homeostasis and adaptation. *Nat. Commun.* **3**, 1012 (2012).

24. Vergés, E., Colomina, N., Garí, E., Gallego, C. & Aldea, M. Cyclin Cln3 is retained at the ER and released by the J chaperone Ydj1 in late G1 to trigger cell cycle entry. *Mol. Cell* **26**, 649–62 (2007).

25. Yahya, G., Parisi, E., Flores, A., Gallego, C. & Aldea, M. A Whi7-anchored loop controls the G1 Cdk-cyclin complex at start. *Mol. Cell* **53**, 115–26 (2014).

26. Dorsey, S. *et al.* G1/S Transcription Factor Copy Number Is a Growth-Dependent Determinant of Cell Cycle Commitment in Yeast. *Cell Syst.* **6**, 539-554.e11 (2018).

27. Blank, H. M., Callahan, M., Pistikopoulos, I. P. E., Polymenis, A. O. & Polymenis, M. Scaling of G1 Duration with Population Doubling Time by a Cyclin in *Saccharomyces cerevisiae*. *Genetics* **210**, 895–906 (2018).

28. Tu, B. P., Kudlicki, A., Rowicka, M. & McKnight, S. L. Logic of the yeast metabolic cycle: temporal compartmentalization of cellular processes. *Science* **310**, 1152–8 (2005).

29. Papagiannakis, A., Niebel, B., Wit, E. C. & Heinemann, M. Autonomous Metabolic Oscillations Robustly Gate the Early and Late Cell Cycle. *Mol. Cell* **65**, 285–295 (2017).

30. Slavov, N., Macinskas, J., Caudy, A. & Botstein, D. Metabolic cycling without cell division cycling in respiring yeast. *Proc. Natl. Acad. Sci. U. S. A.* **108**, 19090–5 (2011).

31. Burnetti, A. J., Aydin, M. & Buchler, N. E. Cell cycle Start is coupled to entry into the yeast metabolic cycle across diverse strains and growth rates. *Mol. Biol. Cell* **27**, 64–74 (2016).

32. Cai, L. & Tu, B. P. Driving the cell cycle through metabolism. *Annu. Rev. Cell Dev. Biol.* **28**, 59–87 (2012).

33. Shi, L. & Tu, B. P. Acetyl-CoA induces transcription of the key G1 cyclin CLN3 to promote entry into the cell division cycle in Saccharomyces cerevisiae. *Proc. Natl. Acad. Sci. U. S. A.* **110**, 7318–23 (2013).

34. Unger, M. W. & Hartwell, L. H. Control of cell division in Saccharomyces cerevisiae by methionyl-tRNA. *Proc. Natl. Acad. Sci. U. S. A.* **73**, 1664–8 (1976).

35. Lee, S. S., Avalos Vizcarra, I., Huberts, D. H. E. W., Lee, L. P. & Heinemann, M. Whole lifespan microscopic observation of budding yeast aging through a microfluidic dissection platform. *Proc. Natl. Acad. Sci. U. S. A.* **109**, 4916–20 (2012).

36. Huberts, D. H. E. W. *et al.* Construction and use of a microfluidic dissection platform for long-term imaging of cellular processes in budding yeast. *Nat. Protoc.* **8**, 1019–27 (2013).

37. Elbing, K. *et al.* Role of hexose transport in control of glycolytic flux in Saccharomyces cerevisiae. *Appl. Environ. Microbiol.* **70**, 5323–30 (2004).

38. Yoshioka, K. *et al.* A novel fluorescent derivative of glucose applicable to the assessment of glucose uptake activity of Escherichia coli. *Biochim. Biophys. Acta* **1289**, 5–9 (1996).

39. Snoep, J. L., Mrwebi, M., Schuurmans, J. M., Rohwer, J. M. & Teixeira de Mattos, M. J. Control of specific growth rate in Saccharomyces cerevisiae. *Microbiology* **155**, 1699–1707 (2009).

40. Youk, H. & van Oudenaarden, A. Growth landscape formed by perception and import of glucose in yeast. *Nature* **462**, 875–9 (2009).

41. Otterstedt, K. *et al.* Switching the mode of metabolism in the yeast Saccharomyces cerevisiae. *EMBO Rep.* **5**, 532–7 (2004).

42. Novak, S., Zechner-Krpan, V. & Marić, V. Regulation of Maltose Transport and Metabolism in Saccharomyces cerevisiae. *Food Technol Biotech* 213–218 (2004).

43. Blount, B. A., Weenink, T., Vasylechko, S. & Ellis, T. Rational diversification of a promoter providing fine-tuned expression and orthogonal regulation for synthetic biology. *PLoS One* **7**, e33279 (2012).

44. Gustavsson, A.-K. *et al.* Sustained glycolytic oscillations in individual isolated yeast cells. *FEBS J.* **279**, 2837–47 (2012).

45. Aon, M. A. *et al.* Dynamic regulation of yeast glycolytic oscillations by mitochondrial functions. *J. Cell Sci.* **99 ( Pt 2)**, 325–34 (1991).

46. Kang, H. T. & Hwang, E. S. 2-Deoxyglucose: an anticancer and antiviral therapeutic, but not any more a low glucose mimetic. *Life Sci.* **78**, 1392–9 (2006).

47. de Felipe, P. *et al.* E unum pluribus: multiple proteins from a self-processing polyprotein. *Trends Biotechnol.* **24**, 68–75 (2006).

48. Edgington, N. P. & Futcher, B. Relationship between the function and the location of G1 cyclins in S. cerevisiae. *J. Cell Sci.* **114**, 4599–611 (2001).

49. Jorgensen, P. *et al.* The size of the nucleus increases as yeast cells grow. *Mol. Biol. Cell* **18**, 3523–32 (2007).

50. Webster, M., Witkin, K. L. & Cohen-Fix, O. Sizing up the nucleus: nuclear shape, size and nuclear-envelope assembly. *J. Cell Sci.* **122**, 1477–86 (2009).

51. Nishimura, K., Fukagawa, T., Takisawa, H., Kakimoto, T. & Kanemaki, M. An auxin-based degron system for the rapid depletion of proteins in nonplant cells. *Nat. Methods* **6**, 917–922 (2009).

52. Papagiannakis, A., de Jonge, J. J., Zhang, Z. & Heinemann, M. Quantitative characterization of the auxin-inducible degron: a guide for dynamic protein depletion in single yeast cells. *Sci. Rep.* **7**, 4704 (2017).

53. Leupold, S. *et al.* Saccharomyces cerevisiae goes through distinct metabolic phases during its replicative lifespan. *Elife* **8**, (2019).

54. Lew, D. J. & Reed, S. I. Morphogenesis in the yeast cell cycle: regulation by Cdc28 and cyclins. *J. Cell Biol.* **120**, 1305–20 (1993).

55. Bryan, A. K., Goranov, A., Amon, A. & Manalis, S. R. Measurement of mass, density, and volume during the cell cycle of yeast. *Proc. Natl. Acad. Sci. U. S. A.* **107**, 999–1004 (2010).

56. Parisi, E., Yahya, G., Flores, A. & Aldea, M. Cdc48/p97 segregase is modulated by cyclin-dependent kinase to determine cyclin fate during G1 progression. *EMBO J.* **37**, e98724 (2018).

57. Futcher, B. Metabolic cycle, cell cycle, and the finishing kick to Start. *Genome Biol.* **7**, 107 (2006).

58. Wullschleger, S., Loewith, R. & Hall, M. N. TOR signaling in growth and metabolism. *Cell* **124**, 471–84 (2006).

59. Lindqvist, L. M., Tandoc, K., Topisirovic, I. & Furic, L. Cross-talk between protein synthesis, energy metabolism and autophagy in cancer. *Curr. Opin. Genet. Dev.* **48**, 104–111 (2018).

60. Moore, S. A. Kinetic evidence for a critical rate of protein synthesis in the Saccharomyces cerevisiae yeast cell cycle. *J. Biol. Chem.* **263**, 9674–81 (1988).

61. Peregrín-Alvarez, J. M., Sanford, C. & Parkinson, J. The conservation and evolutionary modularity of metabolism. *Genome Biol.* **10**, R63 (2009).

62. Bertoli, C., Skotheim, J. M. & de Bruin, R. A. M. Control of cell cycle transcription during G1 and S phases. *Nat. Rev. Mol. Cell Biol.* **14**, 518–28 (2013).

# Methods

## Yeast Strains

Prototrophic *Saccharomyces cerevisiae* strains of the CEN.PK and S288C backgrounds were used in this study. All strains used are listed in Supplementary Table 1. Genomic integrations of fluorescent reporters were carried out using standard PCR-based strategies to amplify resistance cassettes with the respective fluorescent protein and appropriate, typically ≈300-500 bp long, flanking sequences, and C-terminal insertion to the target gene by homologous recombination[63]. Unless indicated otherwise, constructs for TEF1 and Tet-ON driven expression of GFP, as well as for Tet-ON driven expression of Hxt1, were incorporated in the HO genomic locus. The full list of primers and information on how they were used in strain construction are presented in Supplementary Table 2.

## Yeast Growth Media and Procedures

Synthetic minimal media (yeast nitrogen base without amino acids (Formedium) and minimal medium[64] supplemented with the indicated concentrations of glucose, maltose, galactose, or lactate (Sigma-Aldrich) were used throughout. Batch cultivation took place at 30$^{o}$C at a shaking speed of 300 rpm. Cells from log-phase batch cultures were used to load the microfluidics device, and thereafter, cells were continuously supplemented with fresh medium of the indicated composition. For nutrient shifts during microfluidics cultivation, media were pre-incubated at 30$^{o}$C.

Unless otherwise indicated, for experiments with low (0.01gL$^{-1}$) glucose, cells from late log-phase from high (20 gL$^{-1}$) glucose cultures were used to inoculate low glucose media at an OD of 0.05. After overnight cultivation, cells were loaded to the microfluidics device and were continuously supplemented with fresh low glucose media for 8.5 to 9 hours before the initiation of the experiment to allow for adaptation to the low glucose conditions.

For identification of percentage of wild-type G1 arrested cells as a function of glucose concentration in the microfluidics device, cells for low glucose concentrations (<10 gL$^{-1}$) were grown to log phase in media with 10 gL$^{-1}$ glucose, were then transferred to media with the appropriate low concentration of glucose for ≈4 hours, and were subsequently loaded to the microfluidics device. Upon loading of the microfluidics device, cells were continuously fed with media containing the appropriate concentration of glucose, and were monitored for 12 hours to assess their capacity to progress from G1 to S phase, by observing the appearance of the bud cell. Cells that were already undergoing cell division at the time of loading, were allowed to complete their current cell division cycle before assessed for G1 arrest for the next 12 hours.

For obtaining large daughter cells, wild type cells from log-phase cultures were loaded to the microfluidics device and were allowed to replicatively age for ≈22 hours, before initiating fluorescent measurements. The large daughters of these replicatively-aged mother cells were then used for further analyses.

Microscopy and imaging

Widefield microscopy was performed using a microfluidics dissection platform[36] mounted to inverted fluorescence microscopes (Eclipse Ti-E; Nikon instruments). The temperature was retained constant at 30$^{o}$C using a microscope incubator (Life Imaging Services GmbH). Images were recorded using an iXon Ultra 897 DU-897-U-CD0-#EX camera (Andor Technology Ltd). During brightfield imaging a UV blocking filter was used. Fluorescent measurements were preformed using an LED-based excitation system (pE2; CoolLED Limited). Fluctuations in axial focus during time-lapse imaging were corrected using automated hardware (PFS; Nikon). Fluorescent measurements for estimation of dynamic protein production rates and Whi5 concentration were performed with 100x objectives. Widefield microscopy settings are presented in Supplementary Table 3. Time-lapse confocal microscopy was performed with a Zeiss LSM800 confocal microscope and photomultiplier tubes by Hamamatsu Photonics, using agar slabs perfused in 20 $gL^{-1}$ glucose medium. A 63x oil immersion objective was used. Temperature was kept at 30°C throughout the experiments using an incubator chamber and a controlled heated objective ring. GFP fluorescence for TEF1-sfGFP and Whi5-sfGFP was analysed by excitation with a 488 nm laser (2% light intensity; 0.56 µs dwell-time exposure) and emission was detected using a 490-535 nm band-pass filter. For every imaging position five z-axis planes with a 0.6 µm step were acquired every 5 min.

To avoid photobleaching related artefacts, especially with respect to Whi5 measurements, more photostable fluorescent proteins[65,66] in comparison to what was used earlier[13] were used, and the imaging frequency was adjusted according to the growth conditions, and thus, to the total amount of light received by the fluorescent proteins during G1. On the other hand, in confocal microscopy (where the light intensities used are considerably higher and some degree of photobleaching is inevitable), we corrected our images for photobleaching, as detailed in the *Image Analysis* section.

Image analysis

*Cell segmentation and fluorescence measurements*

Cell segmentation for cell volume and fluorescence intensity measurements were performed using the semi-automated ImageJ plugin BudJ[23] (http://www.ibmb.csic.es/home/maldea). The compartment of the mother and bud cells were segmented independently and the respective cell volumes where thereafter combined[23]. For validation, cell volume and fluorescent measurements were performed for

specific cells also manually using ImageJ[67], assuming that the body of the cell approximates a prolate ellipsoid. Fluorescent intensity measurements were corrected for background autofluorescence before any further analysis, by subtracting the modal fluorescence value of the whole image from the mean cellular fluorescence at each time point. Cell-cycle and cell-size related changes in autofluorescence did not have any significant influence on the measured fluorescence dynamics (Extended Data Figures 2e, 4g and 5a). Unless specified otherwise, total cellular fluorescence was estimated by multiplying the cell volume with the mean cellular fluorescence at each time point. Verification analyses for widefield measurements were performed also by estimating total cellular fluorescence via integrating fluorescence over the whole cell area. In one case where we observed uneven illumination across the y-axis of the field of view, we corrected for this effect by first determining the fluorescence intensity of cells as a function of the y-coordinate of the field of view. Then, since a linear dependency on the y-coordinate of the field of view and the fluorescence intensity was observed, we generated a linear function to describe this dependency, with which we corrected the original image to obtain the flat-field image[68]. Cytokinesis was determined by the darkening of the bud neck on brightfield images[69]. Start was defined as the first time point after the exit of Whi5-GFP or Whi5-mCherry from the nucleus, determined by visual inspection of microscopy images[70]. G1 was defined as the period between cytokinesis and bud appearance. Confocal images analysis was conducted also using ImageJ, BudJ, and a custom-made Python script (available from GitHub at https://github.com/molecular-systems-biology/Litsios-et-al-2019; DOI: 10.5281/zenodo.3455842). Mean cell fluorescence was calculated in all z-axis stacks using the cell boundary detected by BudJ, and pixels with intensity value below the 50-percentile of the whole cell were excluded to avoid erroneous signals from vacuoles. The value of the stack with the maximum mean fluorescence intensity was chosen for further estimations. To correct for photobleaching, the mean GFP fluorescent intensities of every cell at every time point were averaged and a decreasing exponential function was fitted. The function was normalized for its first value (t = 0) and the inverse of the normalized photobleaching function value at each time point was used to correct the original signal from each cell.

*Processing of single-cell time series data*

The time series describing the time evolution of different single-cell quantities were processed with a computational pipeline based on Gaussian processes (GPs), a class of powerful and flexible non-parametric Bayesian models that are used to define distributions over functions[71]. GP-based regression on noisy data combines in a natural way our prior beliefs about features of the underlying function (e.g. smoothness, relevant time scales etc.) with the measurement uncertainty into a posterior probability distribution which reflects the residual uncertainty about the function that gave rise to the observed data. The GP posterior can be used to predict the underlying function values and their

associated uncertainty at any time point. Moreover, since the derivative of a GP is another GP[72], the time-derivative of the measured time-series and be analytically estimated from the GP posterior obtained from the measurements. Further information and background on Gaussian processes can be found in[71,73].

Concretely, our data-processing pipeline for each single-cell quantity (total fluorescence, cell volume, NAD(P)H fluorescence time series) comprised the following steps: (i) Manual inspection of each single-cell trajectory for obvious artefacts, such as those generated by failed mother/bud cell tracking and shifts in focus, which result in large, sudden jumps in measured cell volumes and/or fluorescence. To avoid biasing the results, single-cell trajectories affected by such artefacts were discarded. (ii) GP-based smoothing of each single-cell time series using a GP prior with zero mean and a rational quadratic covariance function[71]. The hyperparameters of the covariance function were estimated by maximizing the marginal likelihood of the measured data using multistart optimization started from 20 random initial points and retaining the best of these runs. At the end of this step, an optimized posterior GP was obtained for every single-cell trajectory. (iii) Calculation of the posterior predictive mean and variance over a dense grid of time points. (iv) Estimation of the mean and variance of the derivative process based on the data of Step (iii). GP fitting (hyperparameter optimization) and posterior-based predictions were carried out using the GPML Matlab toolbox[74]. To estimate derivatives, we used a custom-made Matlab script based on the mathematical results presented in[72].

In order to simplify the analysis and avoid the unnecessary amplification of measurement noise by additional data-processing steps, the maturation half-life of sfGFP was assumed to be negligible during the processing of fluorescence measurements. This choice was justified based on estimates of the sfGFP maturation rate, which corresponds to a half-time of about 5 min[75]. Moreover, as demonstrated in[76], taking into account such a short maturation half-life has negligible impact on the estimated protein production kinetics.

2-NBDG based glucose uptake rate assay

For comparing the glucose uptake rate in coexisting G1-arrested and dividing cells of the TM6* strain, cells were cultivated in the microfluidics device in 10 $gL^{-1}$ glucose and subsequently switched to 0.01 $gL^{-1}$ glucose plus 60 µM 2-NBDG for 25 min. The ratio of cellular fluorescence at 470 nm (Supplementary Table 3) right after and before the treatment with 2-NBDG was estimated for both dividing and G1-arrested cells. Cells were identified as G1-arrested if they did not bud for at least 24 hours.

Characterization of TM6* physiology during growth on glucose and maltose

For characterization of TM6* physiology on glucose and maltose, log-phase cultures with the respective carbon source at 10 $gL^{-1}$ concentration were sampled every 60 or 120 min to determine growth by $OD_{600nm}$ measurements and cell count by flow cytometry (BD Accuri C6; BD Biosciences). Levels of glucose or maltose and extracellular metabolites were determined every 60 or 120 min by collecting 0.2 mL of culture and centrifuging for 5 min at 13200 rpm. The cell-free supernatant was transferred to filter columns of 0.22 pore size (SpinX; Corning Inc), spun for 15 s, and the flow-through was transferred to an HPLC vial for HPLC analysis (Agilent 1290 LC System; Agilent Technologies) using a Hi-Plex H column with 5 mM $H_2SO_4$ as eluent at a constant flow rate of 0.6 mL $min^{-1}$ and column temperature of 60°C. Chromatogram integration was done with Agilent Open Lab CDS software. As a reference, the physiology of KOY.PK2-1C83 (wild type) strain was measured in the same way on 10 $gL^{-1}$ glucose. Data were obtained from at least 3 biological replicates for each stain at each tested condition. Dry cell weight was determined by culture filtering through pre-weighed nitrocellulose 0.2 2 µm pore size filters (Whatman; GE Healthcare Life Sciences), and re-weighting after dry-incubation at 80°C. The cell count of the culture right before filtration was used to calculate the dry weight per cell of the examined strain at the respective nutrient condition. Oxygen and carbon dioxide transfer rates were determined every 30 min using the online gas exhaust monitoring system RAMOS (Kühner AG)[77]. For RAMOS measurements, media were inoculated from the same cultures used to inoculate the cultures for the determination of glucose, maltose and ethanol concentrations, and cultivations were run in parallel.

Regression analysis was performed in gPROMS using an exponential growth model consisting of the following equations:

$$\frac{\mathrm{d}}{\mathrm{dt}}\mathrm{X} = \mu * \mathrm{X}$$

$$\frac{dc_S}{dt} = -X * q_S$$

$$q_s = \frac{\mu}{Y_{xs}}$$

For each extracellular metabolite the following equations were used:

$$\frac{dc_P}{dt} = X * q_P$$

$$q_p = \frac{Y_{ps}}{Y_{xs}}$$

Where:

$X$ : $[g_{dcw}/l]$ $biomass\ concentration$

$c_s$ : $[g/l]$ $substrate\ concentration$

$c_p$ : $[g/l]$ $product\ concentration$

μ : $[h^{-1}]$ $biomass\ growth\ rate$

$q_s$ : $[g/(g_{dcw} * h)]$ $specific\ glucose\ uptake\ rate$

$q_p$ : $[g/(g_{dcw} * h)]$ $specific\ production\ rate$

$Y_{xs}$ : $[g_{dcw}/g]$ $biomass\ yield$

$Y_{ps}$ : $[g/g]$ $product\ yield$

Characterization of the Tet-On Hxt1 system

To characterize the tetracycline-inducible HXT1 expression system a log-phase culture (10 $gL^{-1}$ maltose) was centrifuged (4 min; 300 rpm), medium was removed, and cells were resuspended in 1 mL fresh glucose (10 $gL^{-1}$) medium, which was used to inoculate new glucose (10 $gL^{-1}$) cultures containing a range of tetracycline concentrations. Hxt1-GFP fluorescence was followed by flow cytometry every 60 min. Measurements during 3-8 h period after inoculation, during which steady HXT1-GFP expression was achieved, were used to estimate the mean Hxt1-GFP fluorescence per condition. As a control for leaky Hxt1-GFP expression, cultures without tetracycline were followed. As a control for cellular autofluorescence, a culture of *VW100 tet-Hxt1* without tetracycline was followed. To correct for fluorescence of the tetracycline molecules at the GFP spectrum, *VW100 tet-Hxt1* cells were incubated for ≈1 hour in glucose (10 $gL^{-1}$) medium containing all the range of the tested tetracycline concentrations. An effect of tetracycline on cellular autofluorescence was observed at tetracycline concentrations of 200 ng $mL^{-1}$ and higher, and the level of tetracycline-related autofluorescence was subtracted from the *VW100 tet-Hxt1-GFP* measurements at the respective concentrations.

Comparison of single-cell Cln3 measurements with population-based Cln3 data from Blank *et al*. [27]

For Extended Data Figure 4d, the mean concentration of Cln3 during G1 for each cell was measured in cells growing on 20 $gL^{-1}$ glucose (n=41), 20 $gL^{-1}$ galactose (n=36), and 20 $gL^{-1}$ lactate (n=43), and doubling time was estimated by determining the time between cell birth and completion of the first division cycle (cytokinesis) for single cells growing at the respective nutrient conditions (n=36, 29, and 14 respectively). To compare our single-cell Cln3 measurements across different growth conditions with respective population-based measurements of a recent study[27], Cln3 data from Figure 4A from Blank et al (2018) were digitized using PlotDigitizer 2.6.8. For direct comparison with our single-cell data, the mean was calculated for Cln3 levels and doubling times corresponding to measurements from similar doubling times in the study of Blank et al (2018). Specifically, data from the following ranges of doubling times were grouped together: 2.43-2.78 hours, n=7; 3.05-3.09 hours, n=3; 7.99-8.14 hours, n=3.

Measurement of Cln3 and Whi5 via targeted proteomics in cell-cycle-synchronous cultures

*Elutriation and sampling*

For the targeted proteomics experiments, single wild type colonies were used to inoculate liquid YPD cultures. After overnight growth, cultures were diluted in fresh media at an $OD_{600}$ = 0.5-1 and were allowed to undergo ≈ 2-3 cell divisions before harvested for elutriation. Elutriation was performed similarly as described previously[78]. 100 mL cultures were loaded into a large elutriation chamber (40 mL) at a pump speed of 40 mL*min$^{-1}$ and rotor speed of 3200 rpm. The elutriation buffer was YPD pre-warmed at 30°C. Approximately 300 mL of media containing small-sized cells were collected by increasing the pump speed to 65 mL*min$^{-1}$. The elutriated cells were centrifuged at 3900 rpm for 2 min, re-suspended in 35 mL of pre-warmed YPD and incubated at 30°C with shaking. Sampling took place every 10 minutes. Specifically, 2 ml of culture was centrifuged (30 sec; 11000 rcf), the supernatant was discarded, and cells were flash-frozen in liquid nitrogen. At each time point, 100 uL of culture was also used to measure the cell size distribution of the population using CASY® TT, and 200 uL of culture was fixed with 70% EtOH for determining the budding index via microscopy.

*Sample preparation*

Cell pellets were reconstituted in 40 µL 2% sodium-deoxycholate; 7.5 mM TECEP; 100mM ammoniumbicarbonate and sonicated twice for 10 seconds using a UP200St with VialTweeter (HielscherUltrasonics GmbH). Heat treatment was performed for 10 minutes at 95°C. After cooling, concentration was determined by BCA assay (Thermo, 23252) and 100 µg protein per sample was used for subsequent steps. Alkylation was performed by addition of iodoacetamide to a final concentration of 40 mM and incubation for 45 minutes in the dark at RT. Samples were diluted 1:2 using 100 mM ammoniumbicarbonate, and mass spectrometry grade Trypsin (Promega, V5280) was added at a ratio of 1:50 (µg Trypsin: µg Protein) and incubated overnight at 37°C at 400 rpm. The reaction was stopped by adding trifluoroacetic acid to a final concentration of 1%. Sample cleanup by solid phase extraction was performed with Pierce® C18 tips (Thermo, 87784) according to the supplier's manual. The eluate fraction was dried under vacuum and reconstituted with 20 µL 2% acetonitrile, 0.1% formic acid.

*Targeted PRM-LC-MS analysis of selected peptides/proteins*

In a first step, parallel reaction-monitoring (PRM) assays[79] were generated from a mixture containing 500 fmol of each heavy reference peptide (JPT Peptide Technologies GmbH), iRT KIT peptides according to the manufacturer's protocol (Biognosys, Schlieren, Switzerland), and shotgun data-dependent acquisition (DDA) LC-MS/MS analysis on a Q-Exactive HF platform. The setup of the µRPLC-MS system was as described previously[80]. Chromatographic separation of peptides was carried out using an EASY

nano-LC 1000 system (Thermo Fisher Scientific), equipped with a heated RP-HPLC column (75 µm x 30 cm) packed in-house with 1.9 µm C18 resin (Reprosil-AQ Pur, Dr. Maisch). Peptides were analysed per LC-MS/MS run using a linear gradient ranging from 95% solvent A (0.1% formic acid in water (v/v)) and 5% solvent B (80% acetonitrile, 19.9% water, 0.1% formic acid (v/v/v)) to 45% solvent B over 60 minutes at a flow rate of 200 $nL*min^{-1}$. Mass spectrometry analysis was performed on Q-Exactive HF mass spectrometer equipped with a nanoelectrospray ion source (both Thermo Fisher Scientific). Each MS1 scan was followed by high-collision-dissociation (HCD) of the 10 most abundant precursor ions with dynamic exclusion for 20 seconds. Total cycle time was approximately 1 s. For MS1, $3e^6$ ions were accumulated in the Orbitrap cell over a maximum time of 100 ms and scanned at a resolution of 120,000 FWHM (at 200 $m*z^{-1}$). MS2 scans were acquired at a target setting of $1e^5$ ions, accumulation time of 50 ms and a resolution of 30,000 FWHM (at 200 $m*z^{-1}$). Singly charged ions and ions with unassigned charge state were excluded from triggering MS2 events. The normalized collision energy was set to 28%, the mass isolation window was set to 1.4 $m*z^{-1}$ and one microscan was acquired for each spectrum.

The acquired raw-files were searched against a yeast database (UniProt: download date: 30/10/2014, total of 6,652 entries) by the MaxQuant software (Version 1.0.13.13) using default parameters. The best 6 transitions for each peptide were selected automatically using an in-house software tool and imported to Spectrodive software (version 7.5). A mass isolation lists containing 2 peptides for each protein was exported from Spectrodive and imported into the Orbitrap Fusion Lumos operating software for PRM analysis. The complete list of peptides and transitions used for PRM analysis are shown in Supplementary Table 4. Chromatographic separation of peptides was carried out using an EASY nano-LC 1200 system (Thermo Fisher Scientific), equipped with a heated RP-HPLC column (75 µm x 37 cm) packed in-house with 1.9 µm C18 resin (Reprosil-AQ Pur, Dr. Maisch). For PRM analysis, peptide samples were prepared as described above and spiked with the heavy reference peptide mix above at 2 fmol/peptide/ug of total peptide mass. The peptides were separated using a following stepwise gradient: from 95% solvent A (0.1% formic acid in water (v/v)) and 5% solvent B (80% acetonitrile, 19.9% water, 0.1% formic acid (v/v/v)) to 28% solvent B until 45 minutes and then to 45% solvent B until 60 minutes at the constant flow rate of 200 $nL*min^{-1}$. For the PRM-MS analysis (MS2 scans), the resolution of the orbitrap was set to 120,000 FWHM (at 200 $m*z^{-1}$) and the fill time was set to 250 ms to reach a target value of $1e^6$ ions. Ion isolation window was set to 0.4 Th. For each MS cycle, a full MS1 scan at 60,000 FWHM (at 200 $m*z^{-1}$) was included. In addition, a few selected samples were also analyzed in DDA mode using the same LC gradient and parameters as above. After database searching (using MaxQuant and parameters as above) proteotypic peptides for three abundant yeast proteins (Glyceraldehyde-3-phosphate dehydrogenase 3, Enolase 2 and Actin, two peptides for each

protein) were extracted and used for normalizing the PRM results for starting material variations (details see below).

*Quantitative analysis*

The PRM files were imported and processed using the Spectrodive software with the default settings. For each target peptide, the total peak areas of the most intense transitions were exported. Only peptides with the Elution Group Q.Value <0.01 were considered for quantitative analysis. Subsequently, the raw files were imported into the Skyline software (version 4.2) to extract and sum the MS1 intensities of peptide ions belonging to constitutively expressed proteins (Glyceraldehyde-3-phosphate dehydrogenase 3, Enolase 2 and Actin, two peptides for each protein were selected). PRM (MS2) intensities of target peptides were then normalized to the summed (MS1) intensity of selected peptides from the constitutively expressed proteins. The obtained normalized intensities were divided by the median of all samples to shift the final expression values into a meaningful scale of around 1. The mean of the different peptides from each protein was then estimated for each time point for each replicate experiment.

Dynamic depletion of Cln3 in single cells

The uncoupling of Cln3 levels from the overall protein production dynamics was performed as described in Figure 5e, by tagging the endogenous Cln3 with an auxin-inducible degron (AID)[48,49], and using either 1 or 2 mM of the synthetic auxin substitute naphthalene-acetic acid (NAA) to activate depletion. To allow for sufficient activation of depletion, G1 duration was estimated for both Cln3-AID and control, in cells that entered G1 either 15 or 30 min after addition of NAA (1 or 2 mM respectively).

The effect of protein degradation on protein abundance dynamics

Consider a simple model of protein synthesis and degradation. In this model, the abundance of a protein P (denoted by $p$) follows the rate equation

$$\frac{dp}{dt} = k_p(t) - k_d p, \qquad (1)$$

where $k_p(t)$ is the (possibly time-varying) synthesis rate and $k_d$ the degradation rate. We consider two limiting situations: one in which $k_d$ is very large, leading to a very short protein half-life, and one in which $k_d = 0$, corresponding to a highly stable protein such as GFP.

To understand the dynamics of $p(t)$ for large $k_d$, we can turn to the analysis of the linear system (1) in the frequency domain[81]. Viewing the synthesis rate $k_p(t)$ as the system input and $p(t)$ as the output, frequency-response theory tells us that the output will closely track input signals with frequency content smaller than the *bandwidth* of the system, which ranges from the zero frequency up to $f_{BW} = k_d/2\pi$ (corresponding to a period of $k_d^{-1}$). As $k_d$ increases, the range of frequencies over which the

output will be proportional to the input will increase as well. To get a sense of the relevant time scales, for a protein with half-life of 5 minutes ($k_d = \log(2)/5 = 0.139\ min^{-1}$) the protein abundance will very closely track inputs that vary over time scales *longer* than $k_d^{-1} = 7.2\ min$.

Put in more intuitive terms, when $k_d$ is very large, the protein abundance tends to equilibrate very fast in response to changes in the synthesis rate. For a fixed synthesis rate, $k_{p,0}$, the equilibrium protein abundance is equal to $k_{p,0}/k_d$ . Consequently, for a time-varying synthesis rate and large $k_d$, protein abundance will be very close to $k_p(t)/k_d$. This is result is also known as the *quasi steady-state approximation* [81] in the theory of chemical kinetics. Finally, it should be noted that keeping $k_p(t)$ the same, increasing $k_d$ will also decrease the average levels of the protein.

When $k_d = 0$, equation (1) shows that $p(t)$ will be given by

$$p(t) = p(0) + \int_0^t k_p(s)ds,$$

where $p(0)$ is the amount of protein present at time zero. The stark contrast between the responses of eq. (1) in the two limiting cases (large vs. zero $k_d$) is displayed in Extended Data Figure 8.

Statistics and Reproducibility

Statistical analyses were performed using Matlab and GraphPad Prism. Whenever applicable, two-sided statistical tests were performed. Experiments related to Figure 1d and Extented Data Figure 4b were performed once with multiple imaging positions. Overall, sample sizes, measures of centrality and dispersion, statistical tests and p-values, are reported when applicable in the figures and their respective captions. For non-graphically reported data, this information is included in the main text.

**Data Availability**

Source data for Figures 1-6 and Extented Data Figures 1-8 are provided in Source Data. The mass spectrometry proteomics data have been deposited to the ProteomeXchange Consortium via the PRIDE[82] partner repository with the dataset identifier PXD015327. All other data are available from the authors on resonable request.

**Code Availability**

At https://github.com/molecular-systems-biology/Litsios-et-al-2019 (DOI: 10.5281/zenodo.3455842), we provide one CSV file with raw microscopy data together with the respective Matlab file in which the data processing (smoothing, rate estimation etc.) is performed, as an example of our data processing pipeline. These data were used in the construction of Fig. 5c of the main text and

Extended Data Figure 4h. The custom-made Python script used for analysis of confocal images is also provided. All other Matlab scripts used for processing are available from the authors on reasonable request.

**REFERENCES**


63. Wach, A. PCR-synthesis of marker cassettes with long flanking homology regions for gene disruptions in S. cerevisiae. *Yeast* **12**, 259–65 (1996).

64. Verduyn, C., Postma, E., Scheffers, W. A. & Van Dijken, J. P. Effect of benzoic acid on metabolic fluxes in yeasts: a continuous-culture study on the regulation of respiration and alcoholic fermentation. *Yeast* **8**, 501–17 (1992).

65. Shaner, N. C., Steinbach, P. A. & Tsien, R. Y. A guide to choosing fluorescent proteins. *Nat. Methods* **2**, 905–909 (2005).

66. Shaner, N. C. *et al.* A bright monomeric green fluorescent protein derived from Branchiostoma lanceolatum. *Nat. Methods* **10**, 407–9 (2013).

67. Schindelin, J. *et al.* Fiji: an open-source platform for biological-image analysis. *Nat. Methods* **9**, 676–82 (2012).

68. Waters, J. C. Accuracy and precision in quantitative fluorescence microscopy. *J. Cell Biol.* **185**, 1135–48 (2009).

69. Zopf, C. J., Quinn, K., Zeidman, J. & Maheshri, N. Cell-cycle dependence of transcription dominates noise in gene expression. *PLoS Comput. Biol.* **9**, e1003161 (2013).

70. Doncic, A., Falleur-Fettig, M. & Skotheim, J. M. Distinct interactions select and maintain a specific cell fate. *Mol. Cell* **43**, 528–39 (2011).

71. Rasmussen, C. E. & Williams, C. K. I. *Gaussian processes for machine learning*. (MIT Press, 2006).

72. Swain, P. S. *et al.* Inferring time derivatives including cell growth rates using Gaussian processes. *Nat. Commun.* **7**, 13766 (2016).

73. MacKay, D. J. C. *Information theory, inference, and learning algorithms*. (Cambridge University Press, 2003).

74. Rasmussen, C. E. & Nickisch, H. Gaussian Processes for Machine Learning (GPML) Toolbox. *J. Mach. Learn. Res.* **11**, 3011–3015 (2010).

75. Khmelinskii, A. *et al.* Tandem fluorescent protein timers for in vivo analysis of protein dynamics. *Nat. Biotechnol.* **30**, 708–14 (2012).

76. Wang, X., Errede, B. & Elston, T. C. Mathematical analysis and quantification of fluorescent proteins as transcriptional reporters. *Biophys. J.* **94**, 2017–26 (2008).

77. Anderlei, T., Zang, W., Papaspyrou, M. & Büchs, J. Online respiration activity measurement (OTR, CTR, RQ) in shake flasks. *Biochem. Eng. J.* **17**, 187–194 (2004).

78. Rosebrock, A. P. Synchronization of Budding Yeast by Centrifugal Elutriation. *Cold Spring Harb.*

*Protoc.* **2017**, pdb.prot088732 (2017).

79. Peterson, A. C., Russell, J. D., Bailey, D. J., Westphall, M. S. & Coon, J. J. Parallel reaction monitoring for high resolution and high mass accuracy quantitative, targeted proteomics. *Mol. Cell. Proteomics* **11**, 1475–88 (2012).

80. Ahrné, E. *et al.* Evaluation and Improvement of Quantification Accuracy in Isobaric Mass Tag-Based Protein Quantification Experiments. *J. Proteome Res.* **15**, 2537–47 (2016).

81. Del Vecchio, D. & Murray, R. M. *Biomolecular feedback systems*. (Princeton University Press Princeton, NJ, 2015).

82. Perez-Riverol, Y. *et al.* The PRIDE database and related tools and resources in 2019: Improving support for quantification data. *Nucleic Acids Res.* **47**, D442–D450 (2019).